Shortwave Aerosol Radiative Forcing from MODIS and CERES Observations over the Oceans

Sundar A. Christopher* and Jianglong Zhang

Department of Atmospheric Sciences
University of Alabama, Huntsville

Submitted to

Geophysical Research Letters
January 25, 2002

Revised version submitted: March 1, 2002

* Author to whom correspondence should be addressed
Sundar A. Christopher
Department of Atmospheric Sciences, NSSTC
University of Alabama in Huntsville
320 Sparkman Drive
Huntsville, AL 35806
Phone: (256) 961 – 7872
Fax: (256) 961 – 7755
Email: sundar@nsstc.uah.edu

Abstract

Using spatially and temporally collocated data sets from the Clouds and Earth's Radiant Energy System (CERES) and Moderate-Resolution Imaging Spectroradiometer (MODIS) instruments on the Terra satellite, a new strategy is presented for studying the Shortwave Aerosol Radiative Forcing (SWARF) over the global oceans for September 2000. Using collocated data, the global averaged optical thickness ($\tau_{0.55}$) for cloud-free CERES pixels is 0.07 with a SWARF of -6 Wm^{-2}. The spatial patterns of tropospheric aerosols are clearly seen from satellite observations. The $\tau_{0.55}$ and SWARF values derived from two independent instruments are in excellent agreement with the following relationship: SWARF = $0.35 - 105.34\tau_{0.55} + 61.47\tau_{0.55}^2$ $(0 \le \tau_{0.55} \le 0.7) Wm^{-2}$. The synergistic use of the MODIS and CERES data sets can be used to provide independent estimates of SWARF, and can be used as a validation tool for studies that attempt to model the role of aerosols on climate.

1. **Introduction**

Aerosols play a key role on the radiation balance of the earth-atmosphere system. The study of the radiative effects of tropospheric aerosols including mineral dust, organic carbon, black carbon, and sulfate have proved to be a challenging task due to the spatial and temporal variability of aerosol distribution and its properties. Current estimates of Shortwave Aerosol Radiative Forcing (SWARF) for biomass burning and fossil fuel aerosols range from -0.1 to -0.5 Wm^{-2} and -0.1 to -1.0 Wm^{-2} respectively, and the sign and magnitude of the radiative effect is still uncertain [*IPCC*, 2001]. Typical approaches for studying the radiative forcing of aerosols include: (1) Use of radiative transfer equations to calculate radiative forcing of optically thin aerosols [*e.g. Penner et al.*, 1992]; (2) Use of General Circulation Models (GCM) [*e.g. Hansen et al.*, 1998]; and (3) Use of satellite-derived aerosol distributions and aerosol optical thickness (τ) to calculate the effect of aerosols in radiative transfer models [*e.g. Christopher et al.*, 2002]. Recently, several studies have shown the potential of satellite-retrieved top-of-the-atmosphere (TOA) fluxes to examine the radiative effect of aerosols. *Haywood et al.*, [1999] compared TOA shortwave (SW) fluxes derived from the Earth Radiation Budget Experiment (ERBE) and a GCM model to study the radiative effect of aerosols. *Christopher et al.,* [2000] studied the radiative effect of biomass burning over Central America by using collocated Clouds and Earth's Radiant Energy System (CERES) and Visible Infrared Scanner (VIRS) measurements from the Tropical Rainfall Measuring Mission (TRMM) platform. Using VIRS and CERES data, *Loeb and Kato* [2002] have extended this approach to study the direct radiative forcing of aerosols over the oceans. This approach of using combined satellite measurements provides an independent method for studying the impact of aerosols on climate. NASA's suite of well-calibrated sensors on the Terra satellite provides an unprecedented opportunity to study the effect of aerosols on climate. In this paper, we estimate the SWARF in cloud free regions over the global oceans using a combination of CERES and Moderate-Resolution Imaging Spectroradiometer (MODIS) data sets from Terra.

2. Data and Methodology

Three data sets are used in this study; the MODIS Level 2 (MOD04) daily aerosol product [*Tanré et al.,* 1997; *Kaufman et al.,* 1997]; the MODIS Level 2 daily (MOD06) cloud product [*Ackerman et al.*, 1998], and the pixel level CERES ES-8 at a spatial resolution of 30km at nadir [*Wielicki et al.,* 1996]. The MOD04 and MOD06 provide aerosol and cloud properties and CERES ES-8 data provides TOA SW fluxes. The CERES ES-8 data contains broadband TOA SW (0.3-5 μm) and longwave (5.0-50.0 μm) fluxes that are inverted from measured radiances using Angular Distribution Models (ADM's) developed for the Earth Radiation Budget Program (ERBE) program [*Wielicki and Green,* 1989; *Wielicki et al.,* 1996]. Errors in scene misidentification are estimated to be on the order of 14% [*Dieckmann and Smith,* 1989]. Although the ES-8 do not include aerosol specific ADM's, recent research shows that the uncertainties in using ERBE ADM's instead of ADMs for biomass burning aerosols over land is on the order of 10% [Li et al. 2000]. In this study, since we use only cloud-free CERES pixels over oceans, we expect the uncertainties to be less than 10%.

Using measured radiances at 500m spatial resolution from six bands between 0.55-2.1 μm, the primary aerosol products retrieved by the MODIS algorithm include spectral aerosol optical thickness, the aerosol effective radius (r_e), and the fraction of the total optical thickness contributed by the sub-micron size mode aerosol [*Tanré et al.,* 1997]. These aerosol properties are then reported at 10km spatial resolution in the MOD04 data. The MODIS aerosol optical thickness retrieval over ocean is implemented using a look-up-table approach with 11 sets of aerosol models as inputs [*Tanré et al.,* 1997]. Based on theoretical sensitivity studies, the uncertainties in $\tau_{0.55}$ retrievals are estimated to be $\pm$ 0.05 $\pm$ 0.05$\tau_{0.55}$ over ocean [*Tanré et al.,* 1997]. The MODIS aerosol optical thickness product has been validated against sunphotometer derived values over oceans and recent results have confirmed that the MODIS algorithm over ocean areas is performing within the expected accuracy [*Remer et al.,* 2002b].

The MOD06 product provides cloud top parameters, such as cloud top pressure and cloud top temperature, at 5 km resolution and cloud optical parameters, such as cloud optical thickness and cloud effective radius, at 1 km resolution [*King et al.,* 1992; *Ackerman et al.,* 1998]. The MOD06 data also provides cloud fraction at both 1 and 5 km resolution. In this study, we take each CERES footprint and collocate the 5km- MOD06 data to identify cloud-free regions. For these cloud free regions, we obtain aerosol properties from the MOD04 data. Twenty-nine days of global CERES and MODIS (MOD04 and MOD06) data in September 2000 were used in this study (CERES ES-8 data from September 17th was unavailable) and is roughly equivalent to about 500GB of data.

On Terra, there are two identical CERES instruments. One instrument operates in a cross track scan mode similar to that of the ERBE scanner while the second instrument operates in a biaxial scan mode to provide new angular flux information [*Wielicki et al.,* 1996]. In this study, only the cross track scan mode data is used. The CERES pixels that are labeled as “clear ocean” by the CERES ES-8 data [*Wielicki and Green,* 1989] were first selected. However, due to the large footprint of the CERES scanner, these pixels could still have some cloud contamination. To eliminate these cloud effects, the MOD06 data is collocated with the CERES data and only those CERES pixels with a 0% cloud fraction as identified by the MOD06 data were used. By using such a stringent cloud screening criteria, it is possible that thick aerosol plumes are rejected in the analysis.

The SWARF* at the top of the atmosphere (TOA) is defined as the difference between clear (F_{clr}) and aerosol (F_{aer}) fluxes [*Christopher et al.*, 2000]. In this study, F_{clr} and F_{aer} were averaged over 2°×2° (latitude×longitude) bins. The F_{aer} values are obtained by averaging the cloud free CERES ES-8 data within a 2°×2° bin. However, F_{clr} is more difficult to obtain because when aerosol loading is low, satellite imagers are not effective in detecting *aerosols [Remer et al.*, 2002a]. *Tanré et al.*, [1997] estimated the uncertainties in MOD04 aerosol optical thickness product to be $\pm 0.05 \pm 0.05\tau$ over ocean. In this study, on an average, the SW flux increases by about $5Wm^{-2}$ when the MODIS $\tau_{0.55}$ changes from values near zero to values near 0.05. On a regional basis, *King et al.*, [1999] estimated that the uncertainties in MODIS aerosol optical thickness retrievals over ocean is $0.01 \pm 0.05\tau$ for selected cases during the Tropospheric Aerosol Radiative Forcing Observational Experiment (TARFOX). To obtain F_{clr} values, we use cloud free CERES pixels that have $\tau_{0.55} < 0.02$, as determined by the MODIS data. Due to this assumption, our first order estimation shows that the uncertainties in F_{clr} is on the order of $1Wm^{-2}$.

3. Results and Discussion

Figure 1a and 1b show the global distribution of MODIS-retrieved $\tau_{0.55}$ and CERES-derived SWARF for collocated cloud-free MOD04 and CERES ES-8 data over ocean areas. We emphasize that the aerosol optical thickness shown in Figure1a is reported for cloud-free CERES pixels. Therefore some aerosol features are not seen due to the possible cloud contamination and

* SWARF = F_{clr} - F_{aer}, where F_{aer} is the TOA SW flux in aerosol regions, and F_{clr} is the TOA clear sky flux.

stringent cloud screening procedure (see section 2*). Remer et al.*, [2002b] show the full range of aerosol optical thickness for September 2000. For example, smoke from South Africa and pollution from the Indian subcontinent that is seen in *Remer et al.*, [2002b] is not seen in Figure 1a due to cloud contamination or misidentification of aerosol pixels as being cloudy. Therefore the aerosol optical thickness values reported in this study for cloud-free CERES pixels could be smaller than those reported by *Remer et al.*, [2002b]. The spatial distribution of $\tau_{0.55}$ and SWARF derived from two independent sets of measurements are remarkably consistent. Missing data shown in gray is often due to persistent cloud coverage often observed over the West Coast of South America and Africa [*e.g. Albrecht et al.*, 1995], and over the Intertropical Convergence (ITCZ). The spatial distribution of $\tau_{0.55}$ is consistent with previously reported values [*Husar et al.*, 1997; *Remer et al.*, 2002b]. The regions with $\tau_{0.55}$ values greater than 0.15 are dominated by: (1) dust plumes over the Atlantic ocean and the Mediterranean sea originating from North Africa; (2) biomass burning aerosols over the Indian ocean and South Atlantic ocean from South Africa and smoke aerosols over the Indian Ocean from Australia [*e.g. Olson et al.*, 1999]; (3) Pollutant aerosols from East Asia to the North Pacific ocean and from Europe to the North Atlantic Ocean. The averaged $\tau_{0.55}$ and SWARF values are 0.07 (Figure 1a) and -6 Wm^{-2}(Figure 1b) respectively for cloud-free regions as observed by CERES. Superimposed on Figure 1a are six boxes, which represent selected regions over the ocean and are labeled after the closest aerosol source regions (except Remote Ocean). The six areas are (1) South Africa (SA) (0-40°S, 30-50°E), (2) Australia (AUS) (0-20°S, 110-130°E), (3) East Asia (EA) (20-40°N, 110-130°E), (4) North Africa (NAF) (10-30°N, 10-40°W), (5) North America (NAM) (20-40°N, 60-80°W), and (6) Remote Ocean (RO) (20-40°S, 100-120°W).

Figure 1c shows the relationship between MODIS-retrieved $\tau_{0.55}$ versus the CERES-derived

SWARF. The aerosol optical thickness and SWARF derived from two independent methods are highly correlated. The SWARF is most sensitive to $\tau_{0.55}$ changes when $\tau_{0.55}$ is low and less sensitive to $\tau_{0.55}$ changes when the aerosol loading is high. For example, a change in $\tau_{0.55}$ from 0 to 0.05 causes a change in SWARF of -5.1 Wm^{-2} and a change in $\tau_{0.55}$ from 0.45 to 0.5 causes a change in SWARF of -2.3 Wm^{-2}. A second order polynomial fit through data points yields the following relationship: SWARF = 0.35 -105.34$\tau_{0.55}$ +61.47$\tau_{0.55}^2$ ($0 \leq \tau_{0.55} \leq 0.7$) Wm^{-2}. However, this relationship was developed for only one month of data and may change significantly for other months.

Figure 1d shows the $\tau_{0.55}$ versus the cloud-free SW flux for the six selected regions. The globally averaged value is indicated by the solid black line. When the $\tau_{0.55}$ is less than 0.2, the relationship between SWARF and $\tau_{0.55}$ is similar among the different regions (except for NAF) because when aerosol loading is low, the background aerosols are major contributors to SWARF. The NAF region dominated by dust aerosols is most efficient in reflecting incoming solar energy when compared with other regions. The aerosols from the SA and AUS source regions have lower SWARF values when $\tau_{0.55}$ is greater than 0.2. The slopes of $\tau_{0.55}$ vs. SW flux for the SA and AUS regions are very similar, which implies that the aerosols in these two regions have similar radiative properties where the dominant aerosol type is from biomass burning [*Husar et al.*, 1997; *Olson et al.*, 1999]. Recent studies show that the single scattering albedo (ω_o) of dust and smoke aerosols at 0.64 μm is 0.97 [*Kaufman et al.*, 2001] and 0.86 [*Reid et al.*, 1998] respectively. The higher ω_o values of dust leads to higher TOA SW values when compared with SW flux values for regions dominated by biomass burning and pollutant aerosols. The slope of $\tau_{0.55}$ vs. SW flux for the EA region is between that of dust and smoke regions. The dominant aerosol type is from industrial pollution that has different aerosol radiative characteristics when compared with dust and smoke aerosols.

Table 1 summarizes the results for the six regions. The lowest averaged $\tau_{0.55}$ of 0.039 is observed over the RO region with a SWARF value of -1.73 Wm^{-2}. The highest averaged $\tau_{0.55}$ of 0.17 is found near Australia with a SWARF value of -13.37 Wm^{-2}. The EA and SA regions have similar $\tau_{0.55}$ and SWARF values. However, the NAF region has a SWARF value of -12.56 Wm^{-2}, that is similar to SWARF values over EA and SA regions with a lower $\tau_{0.55}$ of about 0.114. This indicates the differences in aerosol radiative characteristics between regions dominated by dust (NAF), biomass burning (SA), and pollutant aerosols (EA). The aerosol effective radii (r_e) are 1.25 and 1.65 μm for NAF and RO regions respectively. The predominant aerosol type in NAF is dust aerosol with r_e on the order of 1.5-2.5 μm [*Kaufman et al.,* 2001]. The dominant aerosol type over the RO is sea salt, that has a similar or even larger peak effective radius when compared with dust aerosols [*Andreas,* 1998]. In comparison, the r_e values are smaller for SA, AUS, and EA regions because aerosols in these regions are dominated by either smoke or pollutant aerosols with r_e values on the order of 0.1~0.2 μm [*Kaufman et al.,* 1997; *Reid et al.,* 1998].

4. Conclusions

This study shows a new strategy for studying the effect of aerosols on the radiation balance of the earth-atmosphere system through synergistic use of multiple instruments on the same satellite. However, the uncertainties involved in this study should be carefully examined in future studies. One of the uncertainties that arise from this approach is the lack of ADM's for aerosols. New strategies for developing ADM's for aerosols must be developed as a function of aerosol type and optical thickness. The biaxial scan mode data from CERES on Terra can be used to develop such ADM's. Other sources of uncertainty include estimation of F_{clr} in persistent cloudy areas and the effect of surface conditions such as wind speed. The focus of this paper was to examine the global aerosol direct radiative forcing over ocean for cloud free conditions. Averaged over the entire month, for cloud-free CERES pixels, the $\tau_{0.55}$ is 0.07 and SWARF is –6 Wm^{-2}. This is a first step towards the study of global aerosol radiative forcing using satellite measurements. The next challenging step is to extend this work over land regions where the surface effects play an important role. The strengths of other instruments such as the Multi-angle Imaging SpectroRadiometer (MISR) with several view angles can also be utilized to reduce the uncertainties in SWARF.

Acknowledgements

This research was partially supported by NASA grant NCC8-200 under the Global Aerosol Climatology Project. The CERES data were obtained from the NASA Langley Research Center Atmospheric Sciences Data Center and the MODIS data were obtained through the Goddard Space Flight Center Data Center. We also thank the CERES science team for providing the CERES point spread function and geolocation information.

References

Ackerman, S. A., K. I. Strabala, W. P. Menzel, R. A. Frey, C. C. Moeller, and L. E. Gumley, Discriminating clear sky from clouds with MODIS, *J. Geophys. Res., 103*, 32193-32140, 1998.

Albrecht, B. A., C. S. Bretherton, D. Johnson, W. H. Schubert, and A. S. Frisch, The Atlantic Stratocumulus Transition Experiment (ASTEX). *Bull. Am. Meteorol. Soc, 76*, 889-904, 1995.

Andreas, E. L., A new sea spray generation function for wind speeds up to $32 ms^{-1}$, *J. Phys. Oceanogr., 28*, 2175-2184, 1998.

Christopher, S. A, J. Chou, J. Zhang, X. Li and R. M. Welch, Shortwave direct radiative forcing of biomass burning aerosols estimated from VIRS and CERES, *Geophys. Res. Lett., 27*, 2197-2200, 2000.

Christopher, S. A., and J. Zhang, Daytime variation of shortwave direct radiative forcing of biomass burning aerosols from GOES 8 imager, *J. Atmos. Sci*., *59*, 681-691, 2002.

Dieckmann, F. J., and G. L. Smith, Investigation of scene identification algorithms for radiation measurements, *J. Geophys. Res*., *94*, 3395-3412, 1989.

Hansen, J., M. Sato, A. Lacis, R. Ruedy, I. Tegen, and E. Matthews, Climate forcings in the Industrial era, *Proc. Natl. Acad. Sci*., *95*, 12,753-12,758, 1998.

Haywood, J. M., V. Ramaswamy, and B. J. Soden, Tropospheric aerosol climate forcing in clear-sky satellite observations over the oceans, *Science, 283*, 1299-1303, 1999.

Husar R. B., J. M. Prospero, and L. L. Stowe, Characterization of tropospheric aerosols over the oceans with the NOAA advanced very high-resolution radiometer optical thickness operational product, *J. Geophys. Res*., *102*, 16889-16909, 1997.

Intergovernmental Panel on Climate Change (IPCC), Climate change 2001, The scientific basis, *Cambridge University Press,* 881pp, 2001.

Kaufman Y.J., D. Tanré, L. A. Remer, E. Vermote, A. Chu and B. N. Holben, Operational remote sensing of tropospheric aerosol over land from EOS moderate resolution imaging spectroradiometer, *J. Geophys. Res*., *102*, 17051-17067, 1997.

Kaufman Y.J., D. Tanré, O. Dubovik, A. Karnieli, and L.A. Remer, Absorption of sunlight by dust as inferred from satellite and ground-based remote sensing, *Geophys. Res. Lett., 28*, 1479-1482, 2001.

King, M. D., Y. J. Kaufman, W. P. Menzel, and D. Tanre, Remote sensing of cloud, aerosol, and water vapor properties from the Moderate Resolution Imaging Spectrometer (MODIS), *IEEE Trans. Geosci. Remote Sens., 30*, 2-27, 1992.

King, M.D., Y.J. Kaufman, D. Tanré, and T. Nakajima, Remote sensing of tropospheric aerosols from space: Past, Present, and Future, *Bull. Am. Meteorol. Soc*., *80*, 2229-2259, 1999.

Li, X., S.A. Christopher, J. Chou, and R.M. Welch, Estimation of shortwave direct radiative forcing of biomass burning aerosols using angular dependence models. *J. Appl. Meteor., 39*, 2278-2291, 2000.

Loeb, N. G., and S. Kato, Top-of-Atmosphere direct radiative effect of aerosols from the Clouds and the Earth's Radiant Energy System Satellite instrument (CERES), *J. Climate*, in press, 2002.

Olson, J., R., B. A. Baum, D. R. Cahoon, and J. H. Crawford, Frequency and distribution of forest, savanna, and crop fires over tropical regions during PEM-Tropics A, *J. Geophys. Res*., *104*, 5865-5876, 1999.

Penner, J. E., R. E. Dickinson, and C. A. O'Neill, Effects of aerosol from biomass burning on the global radiation budget, *Science*, *256*, 1432-1434, 1992.

Reid, J. S., P. V. Hobbs, R. J. Ferek, D. R. Blake, J. V. Martins, M. R. Dunlap, and C. Liousse, Physical, chemical and optical properties of regional hazes dominated by smoke in Brazil, *J. Geophys. Res*., *103*, 32059-32080, 1998.

Remer, L. A., Y. J. Kaufman, Z. Levin and S. Ghan, Model assessment of the ability of MODIS to measure top of atmosphere direct radiative forcing from smoke aerosols. *J. Atmos. Sci*., 59, 657-667, 2002a.

Remer, L. A., D. Tanré, Y. J. Kaufman, C. Ichoku, S. Mattoo, R. Levy, D. A. Chu, B. N. Holben, O. Dubovik, A. Smirnov, J. V. Martins, R. R. Li, and Z. Ahmad, Validation of MODIS aerosol retrieval over ocean, *Geophys. Res. Lett.*, (2002b, in press).

Tanré, D., Y.J. Kaufman, M. Herman and S. Mattoo, Remote sensing of aerosol properties over oceans using the MODIS/EOS spectral radiances, *J. Geophys. Res.*, *102*, 16971-16988, 1997.

Wielicki, B. A., B. R. Barkstrom, E. F. Harrison, R. B. Lee III, G. L. Smith, and J. E. Cooper, Clouds and the Earth's Radiant Energy System (CERES): An Earth observing system experiment, *Bull. Am. Meteorol. Soc.*, *77*, 853-868, 1996.

Wielicki, B. A., and R.N. Green, Cloud identification for ERBE radiative flux retrieval, *J. Appl. Meteorol.*, *28*, 1133-1146, 1989.

Figure Captions

Figure 1a. Spatial distribution of MODIS $\tau_{0.55}$ over the global ocean for cloud-free CERES pixels. Missing data for cloud cover shown in gray and the six selected regions (see text) are shown in red boxes. Remer et al., [2002] show the full range of MODIS $\tau_{0.55}$.

Figure 1b. Spatial distribution of CERES-derived SWARF over global ocean.

Figure 1c. MODIS retrieved $\tau_{0.55}$ versus CERES SWARF. A second-order polynomial fit is shown by the solid red line.

Figure 1d. Averaged MODIS $\tau_{0.55}$ vs. CERES SW fluxes for six selected regions. Solid black line shows the globally averaged values.

Table 1. Summary of MODIS and CERES derived values for the six selected regions.

Region	Latitude degrees	Longitude degrees	No.*	SWARF Wm^{-2}	τ (0.55μm)	r_e μm
Australia	20S – 0	110E – 130E	19947	-13.37	0.172	0.43
East Asia	20N – 40N	110E – 130E	2479	-12.43	0.143	0.40
North Africa	10N – 30N	40W – 10W	4709	-12.56	0.114	1.25
North America	20N – 40N	80W – 60W	3678	-8.02	0.067	1.13
South Africa	40S – 0	30E – 50E	20075	-12.66	0.139	0.81
Remote Ocean	40S – 20S	120W –100W	4844	-1.73	0.039	1.65

* Number of CERES pixels.

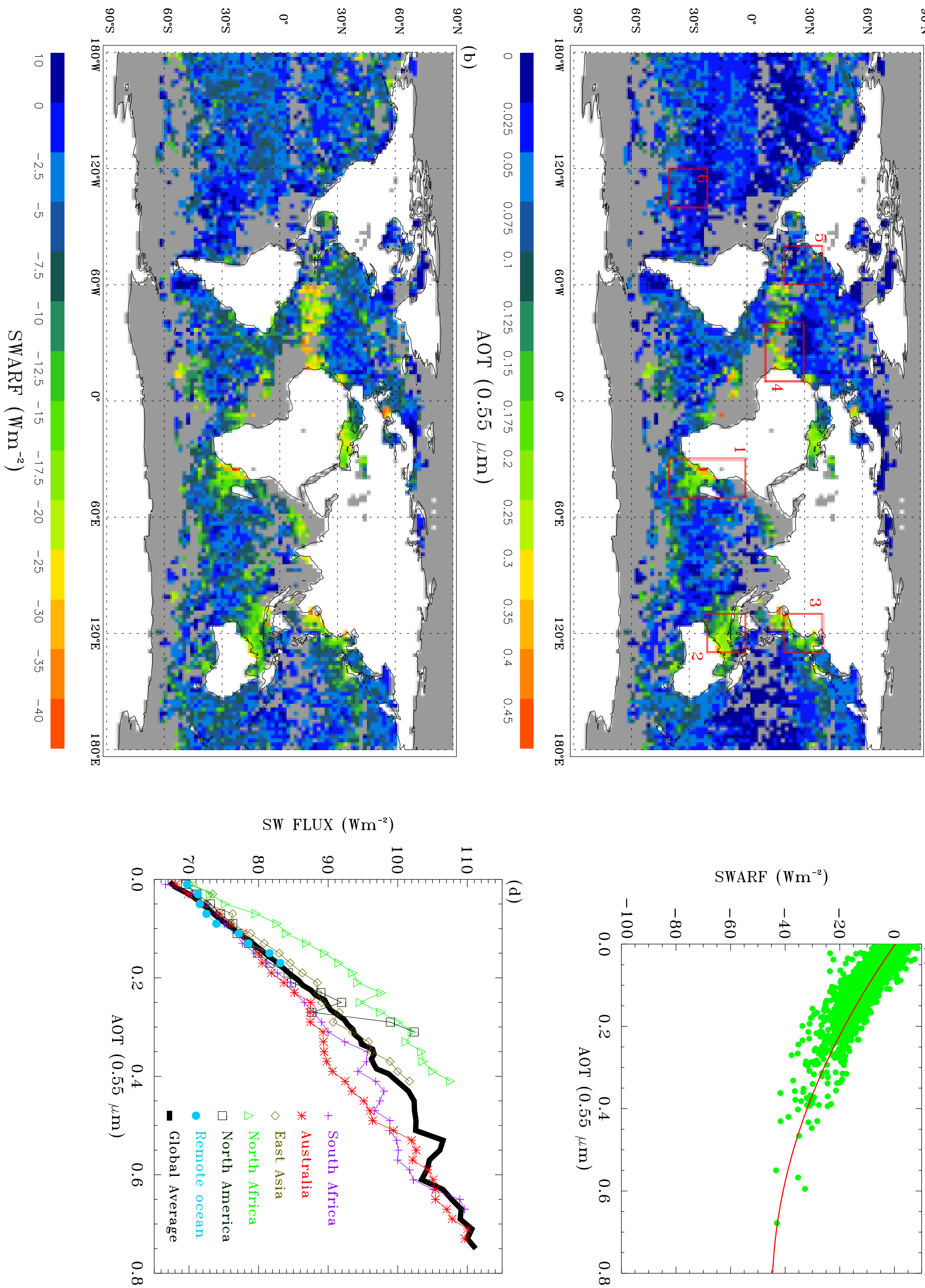
(a)
(b)
(c)
(d)
AOT (0.55 μm)
SWARF (Wm⁻²)
SW FLUX (Wm⁻²)
South Africa
Australia
East Asia
North Africa
North America
Remote ocean
Global Average